Aerospace Science and Technology 92 (2019) 77–90

Contents lists available at ScienceDirect

Aerospace Science and Technology

www.elsevier.com/locate/aescte

Surrogate models for the prediction of the aerodynamic performance of exhaust systems

Giorgio Giangaspero *, David MacManus, Ioannis Goulos

Cranfield University, MK43 0AL Cranfield, Bedfordshire, UK

ARTICLE INFO

Article history:
Received 17 December 2018
Received in revised form 8 May 2019
Accepted 9 May 2019
Available online 14 May 2019

Keywords:
Nozzle performance
Response surface model
Surrogate model
Preliminary design
Exhaust characteristics

ABSTRACT

The aerodynamic performance of the exhaust system is becoming more important in the design of engines for civil aircraft applications. To increase propulsive efficiency and reduce specific fuel consumption, it is expected that future engines will operate with higher bypass ratios, lower fan pressure ratios and lower specific thrust. At these operating conditions, the net thrust and the specific fuel consumption are more sensitive to losses in the exhaust. Thus the performance of the exhaust needs to be accurately assessed as early as possible during the design process. This research investigates low-order models for the prediction of the performance of separate-jet exhaust systems, as a function of the free-stream Mach number, the fan nozzle pressure ratio and the extraction ratio (fan to core pressure ratio). In the current practice the two nozzles are typically considered in isolation and the performance is modelled as a function of their pressure ratio. It is shown that the additional degrees of freedom have a substantial impact on the metrics describing the performance of the exhaust system. These models can be employed at a preliminary design stage coupled with engine performance models, which require as input the characteristics of the exhaust system. Two engines, which are representative of current and future large turbofan architectures are studied. The low-order models investigated, generalized Kriging and radial basis functions, are constructed based on data obtained with computational fluid dynamics simulations. The data represents the characteristics of the exhaust of each engine, and they are provided for the first time for a wide operational envelope. The influence on accuracy of the type of surragate model and its settings have been quantified. Furthermore, the trade-off between the accuracy of the model and the number of samples has been identified. It is found that the exhaust performance metrics can be modelled using a low-order model with sufficient accuracy. Recommendations on the best settings of the model are also provided.

1. Introduction

The current trends in civil aviation are characterized by the drive to reduce specific fuel consumption. This can be achieved by increasing the bypass-ratio and by decreasing the fan pressure ratio and the specific thrust. This strategy, however, leads to configurations for which the specific fuel consumption is more sensitive to losses in the exhaust [1]. Thus, as early as possible in the design process, the performance of the exhaust system needs to be accurately assessed.

This paper focuses on low-order models, also known as response surface models (RSM), for the prediction of the aerodynamic performance of separate-jet exhaust systems. These kind of models are typically employed in industry in a preliminary design phase, linked to engine performance cycle models, to couple the engine characteristics to that of the exhaust. Engine performance cycle models are computer tools used for the prediction of engine performance and fuel burn, and they require as input the characteristics of the exhaust system. The performance of the exhaust system is traditionally quantified through the definition of nondimensional discharge and thrust coefficients, C_D and C_F, respectively, [2–4] (section 2.1). These metrics take into account the internal pressure and viscous drag components in the nozzle stream, which can be substantial sources of thrust loss. The discharge and thrust coefficient relate the performance of the actual nozzle to that of an ideal nozzle that expands isentropically the flow to ambient static pressure [5]. In the current practice the models of C_D and C_F are relatively simple and derived from classical formulations. For instance, a standard characteristic of the nozzle discharge coefficient for a convergent nozzle is a function of the cone half-angle (boat-tail angle) and the nozzle pressure ratio,

* Corresponding author.
E-mail address: g.giangaspero@cranfield.ac.uk (G. Giangaspero).

https://doi.org/10.1016/j.ast.2019.05.027

Nomenclature

Abbreviations

BPR	Bypass Ratio $= \dot{m}^{bypass}/\dot{m}^{core}$ ..... [–]
CFD	Computational Fluid Dynamics
CFL	Courant–Friedrichs–Lewy
CNPR	Core Nozzle Pressure Ratio $= P_0^{core}/p_{amb}$ ..... [–]
CST	Class Shape Transformation
DSFRN	Dual Separate Flow Reference Nozzle
ER	Extraction Ratio FNPR/CNPR $= P_0^{fan}/P_0^{core}$ ..... [–]
FNPR	Fan Nozzle Pressure Ratio $= P_0^{fan}/p_{amb}$ ..... [–]
LOO	Leave One Out
RBF	Radial Basis Function
RMS	Root Mean Square
RSM	Response Surface Model
TSFC	Thrust Specific Fuel Consumption

Subscripts

∞	Relative to the far-field
amb	Ambient
D	Discharge
G	Gross
i	index
N	Net

Symbols

$\dot{m}$	mass flow ..... [kg/s]
γ	ratio of specific heats
ρ	Density ..... [kg/m^3]
σ	standard deviation
A	Area ..... [m^2]
C_F	Thrust coefficient ..... [–]
d	diameter ..... [m]
F	Thrust, propulsive force ..... [N]
n	nugget
p	Static pressure ..... [Pa]
P_0	Total pressure ..... [Pa]
T	Temperature ..... [K]
V	Velocity ..... [m/s]
x	independent variable
y	dependent variable
C_D^{bypass}	Bypass discharge coefficient ..... [–]
C_D^{core}	Core discharge coefficient ..... [–]
C_{F_x}	Overall axial force coefficient ..... [–]
Ma_∞	Free-stream Mach number ..... [–]

Superscripts

core	relative to the core nozzle
fan	relative to the fan nozzle
throat	relative to the throat of the nozzle
*zone*3	relative to the zone3 nozzle

with the discharge coefficient being constant and equal to unity for zero boat-tail angle [6]. The discharge coefficient C_D may be modelled with a monotonic function which depends on the nozzle pressure ratio, on the boat-tail angle and on the diameter ratio [2]. Similarly, the nozzle discharge coefficient can be interpolated from a two-dimensional dataset, with nozzle pressure ratio and nozzle half angle as independent variables [7]. Recent gas turbine models, [8], use the same approach. Furthermore, the influence of the nozzle performance on thrust is typically represented by the thrust coefficient C_F which is defined as the ratio of the actual thrust provided a propelling nozzle to the ideal thrust. The thrust coefficient takes into account that the actual nozzle exit velocity is lower than calculated via isentropic relations due to friction and flow non-uniformity [2]. The nozzle thrust coefficient is often only a function of the nozzle pressure ratio [2,7], or assumed constant [6]. Thus, in all these relatively simple models the influence on performance of the freestream Mach number, which effectively changes the ambient conditions seen by the nozzle, and the influence of the interaction between the two main streams, bypass and core, are not taken into account. It will be shown that these variables have a substantial impact on the performance of the exhaust. For this reason they should not be neglected, especially when considering very high-bypass ratio engines, for which the specific fuel consumption is more sensitive to variations in net propulsive force compared to current engine architectures.

Current large turbofan engines for civil aviation operate with a bypass ratio (BPR) close to 11 [1]. For these engines, the ratio of gross to net propulsive force (F_G/F_N) is approximately 3 [1,9]. At the same time, the exchange rate between exhaust performance and thrust specific fuel consumption (TSFC) is of the order of 3. An improvement of 0.1% in overall exhaust thrust coefficient can result in a reduction of TSFC of roughly 0.3% [10,11]. Future large turbofan engines are expected to be designed with a bypass ratio above 15 [12,1]. This rise in BPR brings an increase in the ratio F_G/F_N, which becomes approximately 4 for a BPR of 16 [1]. This is due to the larger overall mass flow going through the engine which results in an higher inlet momentum drag and higher gross propulsive force. Consequently, the TSFC of future engines is expected to be even more sensitive to changes in thrust coefficient [1]. Furthermore, in order to increase the propulsive efficiency, future engines will operate with lower fan nozzle pressure ratio (FNPR). While current architectures operate with design FNPR of approximately 2.7, future engines will have a FNPR around 2.2 [2,3]. At lower FNPR the flow in the bypass duct can be either choked or unchoked depending on the external conditions. For a given FNPR, the mass flow of an unchoked nozzle is not fixed, thus its discharge coefficient is not constant and it is sensitive to changes in the external conditions. Additionally, the required increase in BPR leads to a higher mass flow exhausted through the bypass duct relative to the core flow. Thus the overall performance of the engine will be more dependent on the design of the bypass nozzle, which could be unchoked over a greater portion of the operating envelope. All these considerations indicate that having accurate models for the prediction of the exhaust performance will be of paramount importance for the design of future turbofan engines.

The performance of an exhaust system can vary greatly from one engine configuration to another. Ideally a model should be able to capture and represent such differences. One way to tackle this requirement is to define classes of engines, defined for instance in terms of ranges of bypass ratios or required thrust, and to pick a particular engine as representative of each class. The underlying assumption is that the exhaust systems of engines belonging to a given class have similar performance, both in terms of trends and absolute values. Thus, in a preliminary design phase, their performance can be represented by one model, i.e. by one engine class. Moreover, the selected representative engines should be optimised geometries. In this work, low-order models for the exhaust systems of two engines (i.e. two classes of engines) for civil aircraft are constructed and studied. The engines considered are representative of current and future large turbofan architectures.

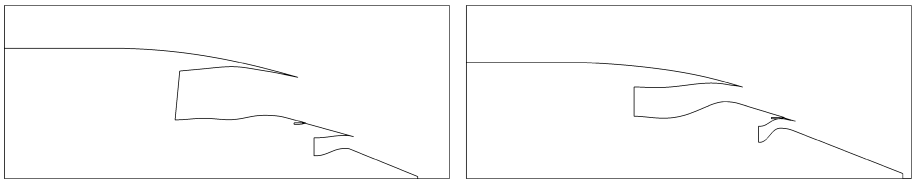

(a) E1 (b) E2

Fig. 1. Two-dimensional axisymmetric representation of the investigated engines architectures. E1 is the engine representative of future architectures and E2 is representative of current architectures.

In this work, Kriging and Radial Basis Functions (RBF) type of models are investigated. In the context of preliminary design and engine performance modelling, these low-order models are attractive as, once generated, they are readily and quickly interrogated. Thus they can be easily integrated into existing engine performance tools and preliminary design systems. The dataset used to build the low-order models is generated by means of computational fluid dynamics (CFD) simulations. The dataset represent the exhaust characteristics of the corresponding engine and they are determined for a wide operational envelope. In addition to the influence of the fan nozzle pressure ratio (FNPR), the influence of the free stream Mach number (Ma_∞) is taken into account. The interaction between the two main streams is also taken into account by considering the extraction ratio (ER = FNPR/CNPR), i.e. the pressure ratio between the fan and core nozzles, as one of the independent variables of the model. In previous works ([11,13]), at least one of the three degrees of freedom was kept constant, and the others varied across a relatively small interval, or with very few samples. Furthermore, previous works focused on engines representative of current architectures (BPR $\approx$10 to 12). In this work, for the first time the characteristics of an engine representative of future large turbofan architectures (BPR $\geq$15) are also presented. The goal is to have a higher fidelity, physics-based representation of the performance of the exhaust system, while still keeping the benefit of a model that can provide a result quickly and therefore can be used in the context of preliminary design.

Surrogate models (or low order models) have been used successfully in many areas of aerospace. For instance, a Gaussian process was developed for preliminary design of aircraft engine nacelles [14]. Kriging and radial basis functions have been investigated for the prediction of the aerodynamic loads (lift, drag and momentum coefficients) of an aircraft [15], focusing on optimal sampling criteria. A gradient-enhanced Kriging model has been developed for the aerodynamic coefficients and drag polar of an RAE 2822 airfoil by combining direct and adjoint CFD solutions [16]. Kriging and gradient-enhanced Kriging models have also been employed in the context of uncertainty quantification [17]. However, to the authors knowledge, they have never been substantially employed in the context of exhaust system performance. Thus the aim of this research work is to assess whether or not Kriging or RBF low-order models can provide a robust and accurate prediction of nozzle characteristics in the context of a preliminary design phase. For each engine the nozzle characteristics are provided for large variations of the independent variables (Ma_∞, FNPR, ER). They constitute novel performance maps used to build surrogate models, the accuracy of which is assessed for the first time for this kind of datasets. Within this context, it is also of interest to provide guidelines regarding the most appropriate settings of the model as well as regarding the number of samples for a given target accuracy. Accuracy requirements are of particular significance when considered alongside the fact that, for future large turbofan architectures (BPR $\geq$15), higher exchange rates are anticipated between exhaust aerodynamic performance and engine TSFC.

Table 1
Engines operating conditions at design point (reproduced from [9]).

Cycle parameters	E1	E2	Unit
FNPR	2.2	2.8	-
ER	1.4	2.0	-
BPR	15+	11	-
Ma	0.85	0.85	-
Altitude	10668	13106	m
Cruise net thrust	$\approx$ 60	$\approx$ 40	kN

2. Background

The representative geometries chosen for this research have been designed and optimised in a previous work [9]. They have been defined in order to be representative of future (E1) and current (E2) large turbofan engines. Their thermodynamic cycles at design-point (mid-cruise) are given in Table 1. The exhaust systems of these geometries have been obtained via a comprehensive optimisation strategy which consists of the following steps: design space exploration (DSE), response surface modelling, and optimisation via genetic algorithm (applied to the surface model) [9]. The optimisation was targeted at the maximisation of the axial force coefficient C_{F_x} (section 2.1). This work focuses on building low-order models to be used in the context of preliminary design. Furthermore, the intention is to replicate a typical industry practice, for which the design effort is dedicated exclusively to the exhaust system, without any detailed knowledge of the nacelle nor of the intake of the engine. Thus, for the purposes of this work, the engines previously designed ([9]) are simplified and a standard exhaust system test configuration is adopted. The 2D axisymmetric geometries of both engines are shown in Fig. 1. This configuration is representative of a typical experimental model exhaust, where the support sting contains the instrumentation and the flow streams that feed the nozzles [13,11,18]. Note that a third smaller ventilation duct, denoted as 'Zone3', is included in the geometry.

2.1. Performance metrics

The metric of interest to describe the performance of the exhaust system are the discharge coefficient (C_D) and the overall axial force coefficient (C_{F_x}). For a given nozzle, the discharge coefficient is defined as:

$$C_d^{nozzle} = \frac{\dot{m}_{actual}}{\dot{m}_{ideal}} \tag{1}$$

where the ideal mass flow is:

$$\dot{m}_{ideal} = A_{throat}\left(\frac{\dot{m}}{A}\right)_{ideal} = \\ = A_{throat} P_0 \left(\frac{1}{\min(\lambda, \lambda_{crit})}\right)^{1/\gamma}$$

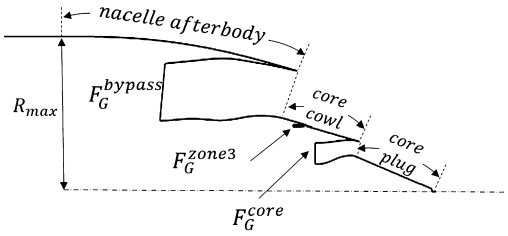

Fig. 2. Illustration of the accounting forces for the gross propulsive force F_G.

$$\times \sqrt{\frac{2\gamma}{(\gamma-1)RT_0}\left(1-\left(\frac{1}{\min(\lambda,\lambda_{crit})}\right)^{\frac{\gamma-1}{\gamma}}\right)} \tag{2}$$

with

$$\lambda = P_0/p_{amb}, \qquad \lambda_{crit} = \left(\frac{\gamma+1}{2}\right)^{\frac{\gamma}{\gamma-1}}. \tag{3}$$

The discharge coefficient gives a measure of the efficiency (i.e. of the losses) of a single duct/nozzle. The overall axial force coefficient C_{F_x} is a global parameter that accounts for the performance of the entire exhaust system [13]. It includes the losses on both internal and external walls up to the point of nacelle afterbody maximum radius R_{max} as well as the gauge stream forces at the inlet of the ducts, see Fig. 2. It is defined as:

$$C_{F_x} = \frac{F_G}{\dot{m}_{actual}^{bypass} V_{ideal}^{bypass} + \dot{m}_{actual}^{core} V_{ideal}^{core} + \dot{m}_{actual}^{zone3} V_{ideal}^{zone3}} \tag{4}$$

where

$$V_{ideal} = \sqrt{\frac{2\gamma RT_0}{(\gamma-1)}\left(1-\left(\frac{1}{\lambda}\right)^{(\gamma-1)/\gamma}\right)} \tag{5}$$

and F_G is the gross propulsive force, defined as the sum of all forces on the walls plus the axial gauge stream forces at the inlet planes of the nozzles:

$$F_G = F_G^{bypass} + F_G^{core} + F_G^{zone3} - \int_{\text{walls}} (p - p_{amb}) \sin\alpha \, \mathrm{d}A - \int_{\text{walls}} (\tau_w \cos\alpha) \mathrm{d}A \tag{6}$$

The variable p indicates the local pressure on the wall, p_{amb} is the ambient static pressure, α is the local surface angle measured from the axial direction, τ_w is the local shear stress and $\mathrm{d}A$ is the infinitesimal surface area. The gauge stream forces are obtained by integrating the axial gauge stream forces across the inlet plane of the corresponding nozzle:

$$F_G^{nozzle} = \int_{\text{inlet}} \rho V_{axial}^2 \mathrm{d}A + \int_{\text{inlet}} (p - p_{amb}) \mathrm{d}A. \tag{7}$$

3. Methodology

3.1. Computational model for the generation of performance maps

The performance maps have been generated via CFD simulations. The computational approach is consistent with previous studies [13,1]. The engines have been parametrised using two dimensional axisymmetric class shape transformation (CST) functions [19], which consist of a class function weighted by a shape function of superimposed Bernstein polynomials, plus an vertical offset. In a normalized Cartesian space $x \in (0, 1)$, defining $x = X/L$ and $y = Y/L$ with L being the axial scale, a CST function can be written as follows:

$$y(x) = C(x) \cdot S(x) + x \cdot y_{\text{offset}}, \quad x \in (0, 1) \tag{8}$$

where $S(x)$ and $C(x)$ are the shape and class function, respectively. The shape function $S(x)$ is defined as

$$S(x) = \sum_{r=0}^{n} \left(A_r K_{r,n} x^r (1 - x^{n-r})\right), \quad K_{r,n} = \frac{n!}{r!(n-r)!} \tag{9}$$

and it corresponds to the $n-$th order Bernstein polynomial

$$BP_n = \sum_{r=0}^{n} \left(K_{r,n} x^r (1 - x^{n-r})\right), \tag{10}$$

scaled by the coefficients A_r. In this work the class function is equal to unity, i.e. $C(x) = 1$ [1]. The bypass as well as the core duct and nozzle aerolines have been reduced to a set of analytical expression as eq. (8). Also analytical expressions are obtained for the external lines, like the nacelle after-body, the core cowl and the plug. As recommended by a previous study [13], the computational domain consisted of a two-dimensional circular far-field with a diameter of $60D$ and an inviscid sting which extends $7D$ upstream from the point of maximum radius of the exhaust system, Fig. 3.

The far-field boundary was modelled with a pressure far-field boundary condition. The static pressure and total temperature imposed at the far-field boundary were kept constant across all numerical simulations. In particular, it was chosen to impose values

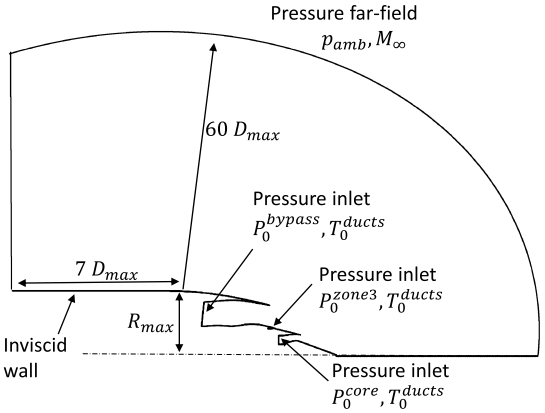

Fig. 3. Computational domain and boundary conditions.

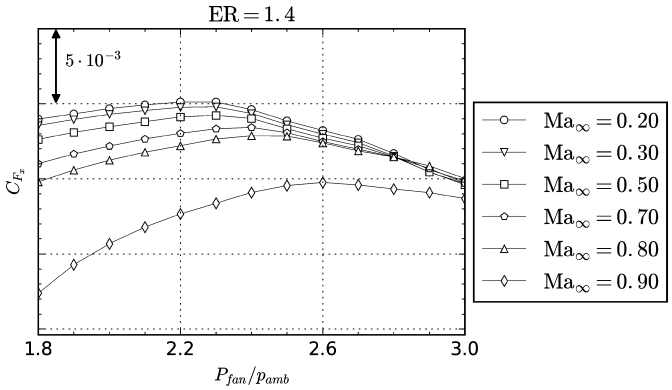

Fig. 4. C_{F_x} for engine E1. Every other datapoint for Ma_∞ and FNPR is shown. Note that only the data relative to ER=1.4 is shown because the variations of C_{F_x} with respect to ER are very small compared to the variations with respect to the other two variables.

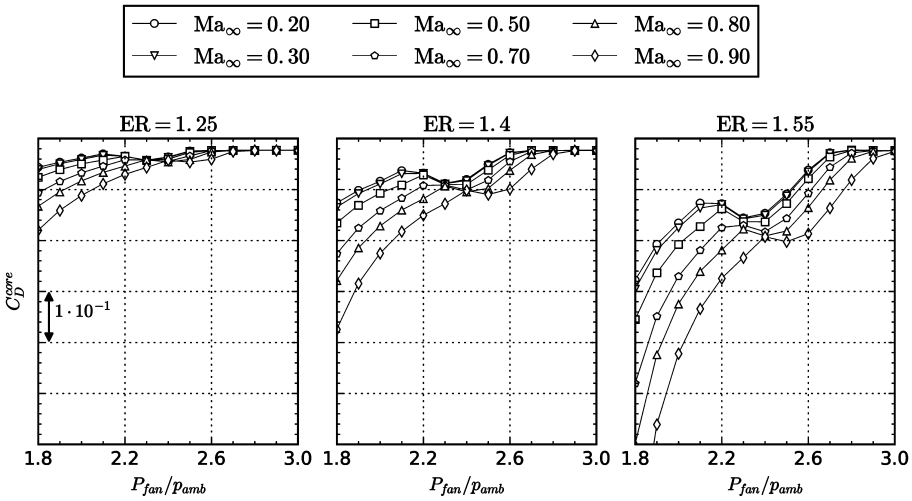

Fig. 5. C_D^{core} for engine E1. Every other datapoint for each variable (Ma, FNPR, ER) is shown.

similar to those used for the Dual Separate Flow Reference Nozzle (DSFRN) benchmark test case ([11,13]). The freestream Mach number was altered via an increased total pressure in the far-field. It was found that the minimum Mach number for which it was possible to obtain a converged solution was 0.02. The inlets of the fan, core and vent streams were modelled with pressure inlet boundary conditions. The inlet total temperature of all three streams was kept constant and equal to $T_0^{ducts} = 294$ K, consistent with the experimental setup of the DSFRN case. The fan and core total pressures were set to achieve the desired fan nozzle pressure ratio (FNPR= P_0^{bypass}/p_{amb}) and extraction ratio (ER= P_0^{bypass}/P_0^{core}), while the total pressure of the zone3 was kept constant and equal to the design value of the given engine. The experimental support sting was modelled as an inviscid (slip) wall. All other walls were modelled as no-slip adiabatic walls.

The computational mesh was generated using a fully structured multi-block approach, with a target y^+ of less than one and 50 nodes in the boundary layer, giving a mesh size of approximately 0.8×10^6 cells. This mesh and a coarser one of $\approx 0.4 \times 10^6$ cells provide a grid convergence index (GCI) [20] of 0.017%, 0.83% and 0.058% for C_D^{bypass}, C_D^{core} and C_{F_x}, respectively [1].

An implicit, density-based, axisymmetric compressible RANS solver was used. All conservation equation were discretized spatially with a second order scheme, and gradients were computed with Green-Gauss node-based discretization. The $k-\omega$ Shear Stress Transport (SST) turbulence model was chosen to close the Favre-averaged equations. The convergence strategy consisted of a gradual increase of the Courant–Friedrichs–Lewy (CFL) number throughout the solution from 0.5 to 40. Residuals of all conserved variables were monitored with convergence of at least four orders of magnitude achieved.

This CFD methodology used in this work has been validated in a previous study ([13]). In previous work by Otter et al. [13] the computational approach was validated with a 3D model of the DSFRN, obtaining a root-mean-square error against the experiments for C_{F_x}, C_D^{bypass} and C_D^{core} of 0.03%, 0.36% and 0.31%, respectively. Similar error levels are found in related works [11]. The trends of all three performance metrics were correctly captured. This CFD approach was then adopted for an axisymmetric representation of the DSFRN configuration [13] where, for a wide range of FNPR, the root-mean-square error against experiments for C_{F_x}, C_D^{bypass} and C_D^{core} was 0.36%, 0.02% and approximately 1.1%, respectively. The higher difference levels of C_{F_x} found for the axisymmetric model were attributed to the lack of the pylon in the axisymmetric model which was included in the 3D model and experimental setup. More details of the validation of the CFD method adopted in this work are presented in Otter et al. [13]. Overall it is considered that the CFD approach is sufficiently validated for the purposes of the current study.

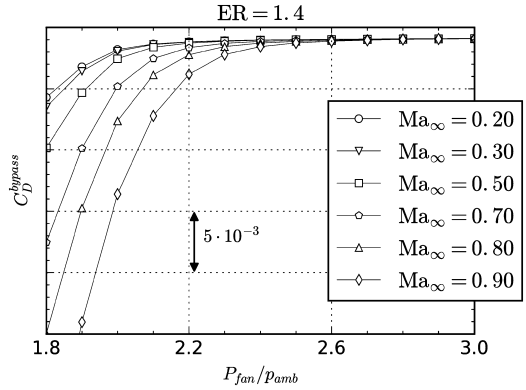

Fig. 6. C_D^{bypass} for engine E1. Every other datapoint for Ma_∞ and FNPR is shown. Note that only the data relative to ER=1.4 is shown because the variations of C_D^{bypass} with respect to ER are very small compared to the variations with respect to the other two variables.

3.2. Performance maps

From the description of the computational approach outlined above (section 3.1), it follows that the numerical simulations are uniquely defined once the freestream Mach number Ma_∞, the FNPR and the ER have been prescribed. These three variables can be varied independently and, for a given geometry, they constitute the degrees of freedom of the problem. The ranges of variation were chosen wide enough to include a typical range of operating conditions.

3.2.1. Engine representative of future architectures E1

The nozzle performance maps for the geometry representative of future large civil aero-engines, E1, are presented in Figs. 4 to 6. The dataset generated for this engine consists of 1625 CFD simulations, obtained with the following sampling strategy: 13 Mach numbers (0.02, 0.1, 0.2, 0.25, 0.3, 0.4, 0.5, 0.6, 0.7, 0.75, 0.8, 0.85, 0.9), 25 FNPR (from 1.8 to 3.0 with steps of 0.05) and 5 ER (from 1.25 to 1.55 with steps of 0.075). This full-factorial sampling strategy enables a better representation of the design space at the boundaries compared to other more advanced strategies, such as Latin Hypercube Sampling (LHS) [21,22] which has been used in

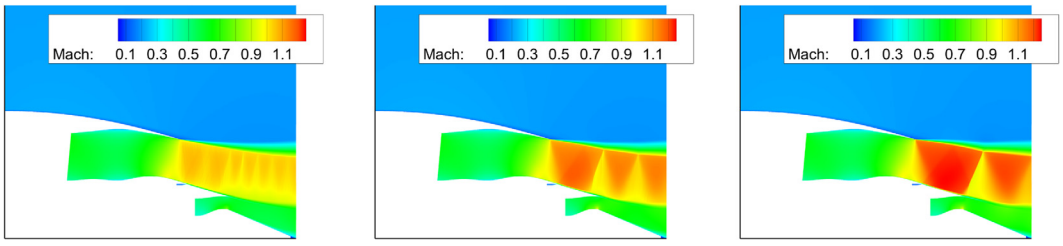

(a) FNPR=2.0 (b) FNPR=2.2 (c) FNPR=2.4

Fig. 7. Mach number contours for E1 at $Ma_\infty = 0.20$, ER = 1.4 and at different FNPR.

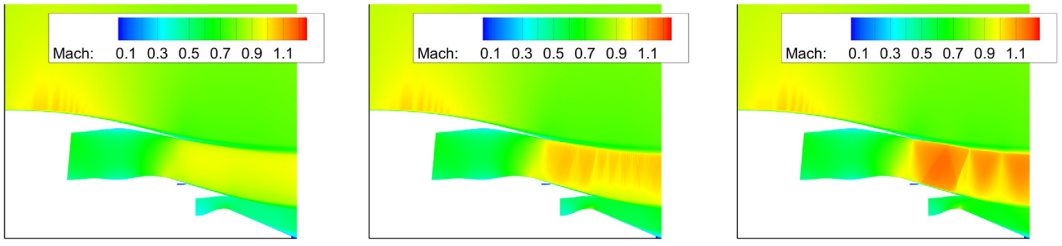

(a) FNPR=2.0 (b) FNPR=2.2 (c) FNPR=2.4

Fig. 8. Mach number contours for E1 at $Ma_\infty = 0.85$, ER = 1.4 and at different FNPR.

previous works [1,9,14]. This is desirable especially when considering Ma_∞, for which the lower bound of the design space is a physical one ($Ma_\infty > 0$) thus it cannot be chosen arbitrarily. Furthermore, it allows appropriate sample resolution for the dominant exhaust parameters. For example, for C_{F_x} the primary variables are FNPR and Ma_∞ (Fig. 4). Finally, this sampling strategy allows the delineation of the effects associated with each of the independent variables (FNPR, ER, Ma_∞), the impact of which can be studied individually. This would not be possible with LHS due to the cross-contamination of the aerodynamic mechanism. This is because with LHS, by construction, no two samples are obtained for the same value of any of the independent variables.

Note that the influence of all three variables ER, FNPR and Ma_∞ is pronounced for C_D^{core}, while the freestream Mach number and the FNPR are the dominating factors for the value of C_D^{bypass} and for C_{F_x}. Furthermore, C_D^{core}, Fig. 5, exhibits the least smooth behaviour compared to the other performance metrics, Figs. 4 and 6. This is because the static pressure field at the exit of the core nozzle is strongly influenced by the shock pattern in the bypass stream as well as by the free stream Mach number (Figs. 7 and 8). The complex pattern of shocks in the bypass stream can create close to the core exit plane a static pressure field characterized by local values considerably higher than the ambient pressure, thus suppressing the mass flow discharged by the core. Furthermore, the shocks are weaker at the higher freestream Mach number, Figs. 7b and 8b. The non-linear nature of the shock formation can cause sudden changes in the behaviour of the core discharge coefficient, which deviates considerably from the classical assumption ([2]) that the discharge coefficient is a monotonic function of the nozzle pressure ratio. Thus the non-linear nature of the underlying problem of a transonic flow in and around a complex geometry translates into the non-linear relationship between the inputs (Ma_∞, FNPR, ER) and the outputs (C_{F_x}, C_D^{bypass}, C_D^{core}) of the model. Non-smooth data might cause unphysical oscillations in the surrogate model if not addressed properly [14], and might cause difficulties in the generation of the RSM. Nevertheless, as shown in section 4, the investigated surrogate models are able to reflect the non-linearity of the problem.

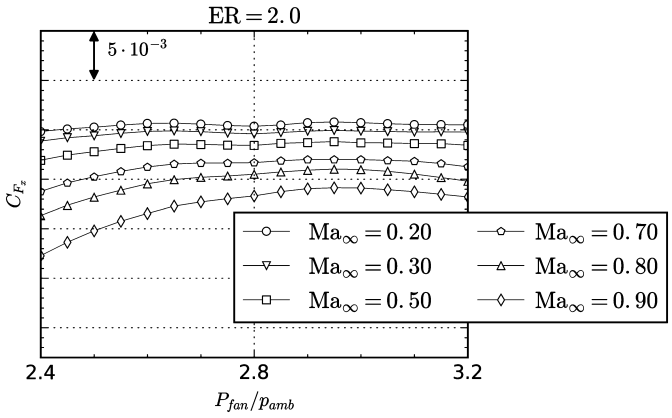

Fig. 9. C_{F_x} for engine E2. Every other datapoint for Ma_∞ and FNPR is shown.

3.2.2. Engine representative of current architectures E2

Engine E2 is representative of current architectures. It has a BPR of 11 and a design FNPR of 2.8 (Table 1). The database of CFD simulations for this engine consists of 663 CFD simulations: 13 Mach numbers (0.02, 0.1, 0.2, 0.25, 0.3, 0.4, 0.5, 0.6, 0.7, 0.75, 0.8, 0.85, 0.9), 17 FNPR (from 2.4 to 3.2 with steps of 0.05) and 3 ER (1.85, 2.0, 2.15). The value of axial force coefficient is almost constant at the higher FNPR, Fig. 9, while for engine E1 there was a clear value of the FNPR for which the C_{F_x} was the largest, for a given ER and Ma_∞. As for engine E1, the metric that exhibits the larger variations is the core discharge coefficient C_D^{core}, Fig. 10. Because this engine's cycle is characterized by much higher FNPR than engine E1, the bypass nozzle is choked over the entire range of data, thus the bypass nozzle discharge coefficient C_D^{bypass} is almost constant. Its value changes of 0.02% over the entire range of conditions.

3.3. Low-order models

The variables (Ma_∞, FNPR, ER) can be varied independently, and for each combination a CFD simulation was run to obtain the performance metrics C_{F_x}, C_D^{bypass} and C_D^{core}. The goal of the work is to construct surrogate models to enable rapid predictions of the performance metrics of a given exhaust system, for a given

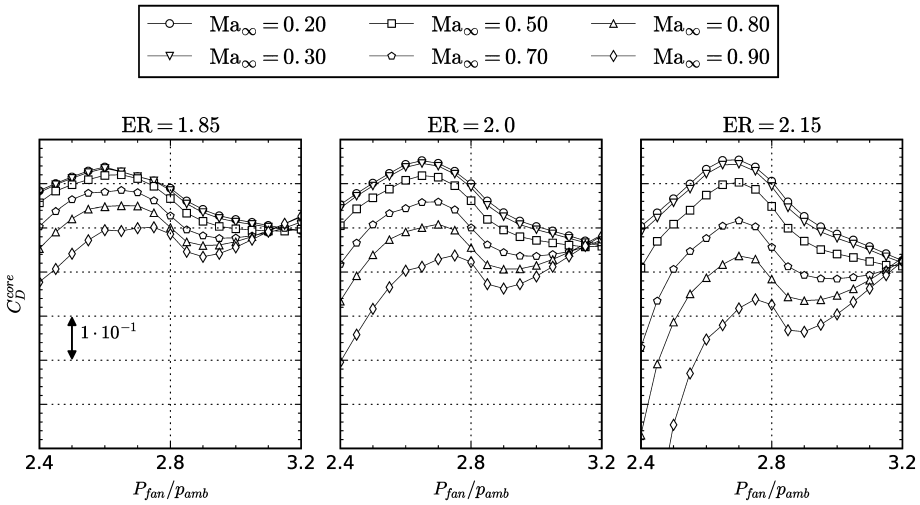

Fig. 10. C_D^{core} for engine E2. Every other datapoint for Ma_∞ and FNPR is shown.

Table 2
Radial basis functions ϕ. r is the local radius and $\bar{r}$ represents the average distance between the data points [25].

multiquadratic	$\sqrt{((r/\bar{r})^2+1)}$
inverse	$1.0/\sqrt{((r/\bar{r})^2+1)}$
gaussian	$exp(-(r/\bar{r})^2)$
linear	r
cubic	r^3
quintic	r^5
thin plate	$r^2 log(r)$

Table 3
Correlation functions $R_i(\theta, w_i, x_i)$ investigated in this work [26,23], with $d_i = w_i - x_i$.

absolute exponential	$exp(-\theta\|d_i\|)$
squared exponential (Gaussian)	$exp(-\theta d_i^2)$
cubic	$1{-}3\chi_k^2 + 2\chi_k^3 \quad \chi_k = min(1, \theta\|d_i\|)$
linear	$max(0, 1{-}\theta\|d_i\|)$

set of (Ma_∞, FNPR, ER). One model was constructed for each performance metric. The models are based on datasets generated with the numerical procedure outlined above in section 3.1. In this work the focus is on two well-known families of response surface models: generalized Kriging, also known as Gaussian process [23], and Radial Basis Functions (RBF) [24].

3.3.1. Radial basis functions

A surrogate model $\tilde{y}$ for the function $y(\mathbf{x})$ constructed with RBFs (ϕ) has the form:

$$\tilde{y}(\mathbf{x}) = \sum_{i=1}^{N} w_i \phi(||\mathbf{x} - \mathbf{x_i}||) = \sum_{i=1}^{N} w_i \phi(r) \tag{11}$$

where N is the total number of points in the dataset, and w_i are the weights of the functions to be estimated under the assumption that the model should recover the original data for all training points. The different types of radial basis functions (ϕ) investigated in this work are those provided by Scip-Py [25] and are summarised in Table 2.

3.3.2. Generalized Kriging

The generalized Kriging model, i.e. Gaussian process, used in this work is that of python package Scikit-learn [26], the implementation of which is based on the work by Lophaven [23]. This implementation offers the ability to specify different regression models, correlation functions, as well as a nugget value (either local or global). A generalized Kriging model approximates the function $y(\mathbf{x})$ with a model $\tilde{y}(\mathbf{x})$ of the form:

$$\tilde{y}(\mathbf{x}) = \mu + z \tag{12}$$

where μ represents a regression model and z a stochastic (random) process assumed to have zero mean and standard deviation σ [23]. The regression models adopted here are linear combinations of known polynomials $f_k(\mathbf{x})$ of order 0, 1 and 2, which give a constant, linear and quadratic regression model, respectively. Given a data set of N samples, the regression model reads:

$$\mu = \sum_{k=1}^{p} \beta_k f_k(\mathbf{x}) \tag{13}$$

where $\beta = (\beta_1, \ldots, \beta_p)$ is the p-dimensional vector of regression coefficients. For instance, for a constant regression model, $p = 1$ and $f_k = f_1 = 1$ and μ reduces to the mean. For a linear regression model, $p = N + 1$ and $f_1 = 1$, $f_2 = \mathbf{x}_1$, $f_{N+1} = \mathbf{x}_N$ [23,15].

The stochastic process has the form:

$$z = \sum_{j=1}^{N} \gamma_j \Gamma(\theta, \mathbf{x}_j, \mathbf{x}) \tag{14}$$

where Γ represents the correlation model between the original j-th data point $\mathbf{x}_j$ and $\mathbf{x}$, multiplied by the coefficients γ_j. The correlation model Γ consists of the products of one-dimensional correlation functions, eq. (15):

$$\Gamma(\theta, \mathbf{w}, \mathbf{x}) = \prod_{i=1}^{dim} R_i(\theta, w_i, x_i) \tag{15}$$

where dim represents the dimensionality of the problem and x_i is the i-th component of the vector $\mathbf{x}$. In this case, since there are three independent variables (Ma_∞, FNPR and ER), $dim = 3$. The correlations function explored here are given in Table 3. The parameters $\beta_k, \gamma_k, \theta$ are determined internally via maximum likelihood estimation. θ is kept constant in the three directions, giving an isotropic model.

The nugget expresses the measure of confidence in the accuracy of a given value. In other words, it is a measure of the noise of the data [22]. It is added to the diagonal of the assumed training covariance and, in the special case of the squared exponential corre-

lation function, the nugget mathematically represents the variance of the input values [26], eq. (16):

$$n = (\sigma_j / x_j)^2 \tag{16}$$

where σ_j is the standard deviation on the j-th input value x_j. The dataset has been generated with the same convergence strategy for all points. Therefore, as first approximation, the uncertainty of the CFD data is considered constant and independent of the boundary conditions. Hence all Kriging surrogate models presented here have been obtained with a constant value of the nugget throughout the design space.

3.3.3. Quality metric

The quality of the RSM is assessed based on the root-mean-square (RMS) of the leave-one-out (LOO) error. The LOO error is based on the classical LOO cross-validation method [27,22]. Given a dataset of N samples, N separate surrogate models are generated. Each separate model is fitted using all N data point except for the one point which the separate RSM in being created for. Then, the separate surrogate model is queried in the left-out point, and this prediction is compared against the original data point. The difference between the two gives a local LOO error, $e_{i,\mathrm{LOO}}$. Thus the selected $N-1$ data points constitute the training sample, while the left-out point is the prediction. This process is repeated for all points and the RMS of the set of local LOO errors is computed, eq. (17), giving a global measure of the quality of the RSM.

$$e_{\mathrm{LOO}} = \sqrt{\frac{1}{N}\sum_{i=1}^{N}(e_{i,\mathrm{LOO}})^2} = \sqrt{\frac{1}{N}\sum_{i=1}^{N}\left(\frac{\tilde{y}_i^{\mathrm{LOO}} - y_i^{\mathrm{CFD}}}{y_i^{\mathrm{CFD}}}\right)^2} \tag{17}$$

The e_{LOO} may be seen as a representative error of a prediction done with the surrogate model in an area of the design space uncovered by the sampling criteria. To put error values in context, it is worth considering how the database of results was built. In this work the database used to train the RSM is computed via CFD simulations, thus an average error of CFD simulations against experiments could be taken as reference. The DSFRN experimental setup [11] is an established test case. Mikkelsen [11] found that the absolute difference between the experimental results of the DSFRN (with a FNPR ranging from 1.4 to 2.6) and a 3D CFD model was between 0.35% and 0.67% for C_D^{bypass}, and between 0.07% and 0.60% for C_D^{core}. Furthermore, the absolute difference in terms of thrust coefficient C_F of the whole exhaust system was between 0.01% and 0.03%. Note that the thrust coefficient C_F as referred to by Mikkelsen [11] takes into account the forces on the pylon, which was present in the experimental setup of the DSFRN. These forces do not appear in the definition of the axial force coefficient C_{F_x} because this refers to the simplified axisymmetric geometries studied in this work. Nevertheless, as the stream forces are the leading terms, the values of thrust coefficient and axial force coefficient are considered comparable. A 3D model of the DSFRN was computed also by Otter [13] and the maximum absolute error was 0.04%, 0.53% and 0.7% for the thrust coefficient C_F, C_D^{bypass} and C_D^{core} respectively. Note that the CFD model and the computational methodology adopted by Otter [13] is similar to the one chosen for this work.

4. Results and discussion

4.1. Kriging

The Kriging model was trained using different regression models, correlation models and nugget value (n, eq. (16)). The influence of the choice of the these settings on the accuracy of the surragate

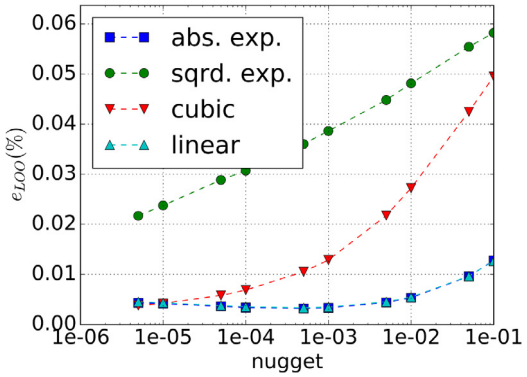

(a) Constant regression function

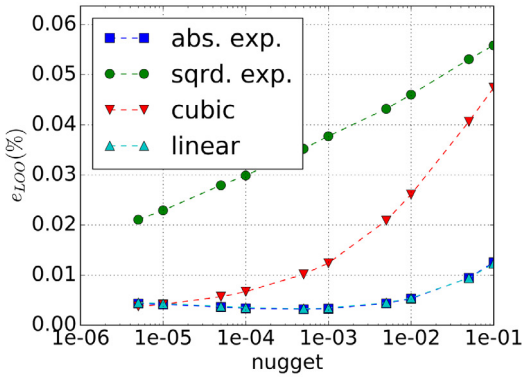

(b) Linear regression function

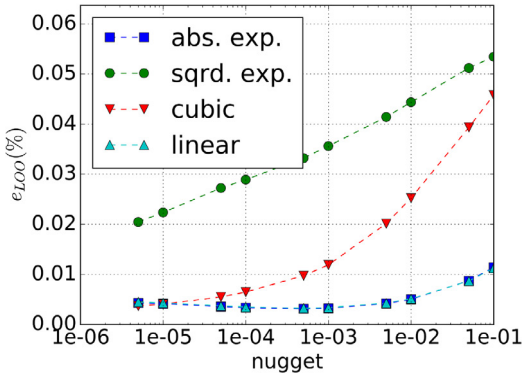

(c) Quadratic regression function

Fig. 11. Influence of regression function, correlation function and nugget value on e_{LOO} of the Kriging model for the axial force coefficient C_{F_x} for engine E1.

models for C_{F_x}, C_D^{bypass} and C_D^{core} is shown in Figs. 11 to 13, respectively, for engine E1.

Decreasing the nugget value is beneficial as it reduces the LOO error e_{LOO} (eq. (17)). Furthermore, the choices of regression and correlation functions are less important compared to the choice of the nugget value (eq. (16)), which can improve substantially the quality of the surrogate model. In particular, the better quality is achieved for very small values of the nugget.

The largest error levels are obtained for the core discharge coefficient C_D^{core} (Fig. 13). For example, the e_{LOO} for C_D^{core} is larger than 0.5% while it is two order of magnitude smaller for C_{F_x} and C_D^{bypass}. C_D^{core} is the metric which exhibits the largest variation across the sample, going from a minimum of 0.1 to a maximum of 0.9, with the minimum values obtained at the lower values of the FNPR and higher values of ER (Fig. 5). Furthermore, C_D^{core} is also the metric whose behaviour is less smooth as it influenced by the suppres-

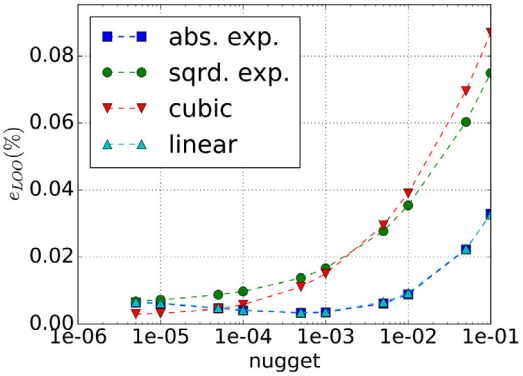

(a) Constant regression function

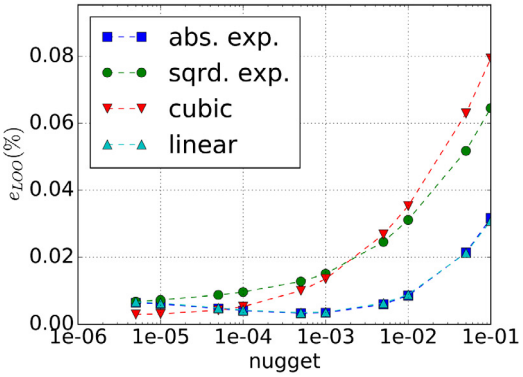

(b) Linear regression function

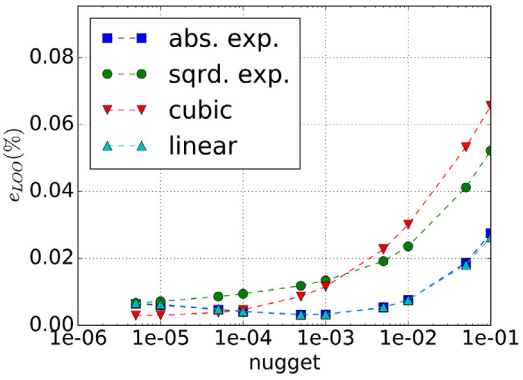

(c) Quadratic regression function

Fig. 12. Influence of regression function, correlation function and nugget value on e_{LOO} of the Kriging model for the bypass discharge coefficient C_D^{bypass} for engine E1.

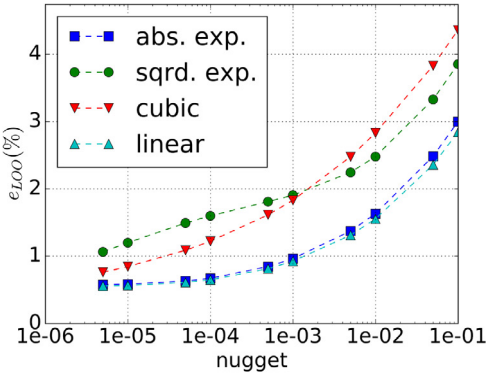

(a) Constant regression function

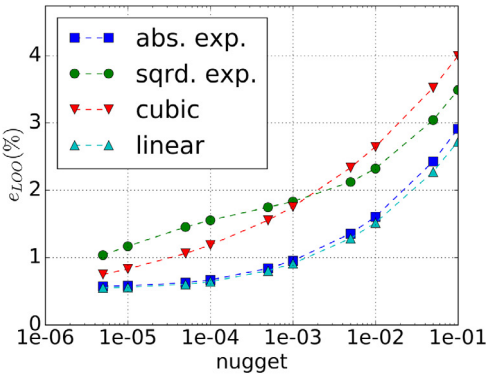

(b) Linear regression function

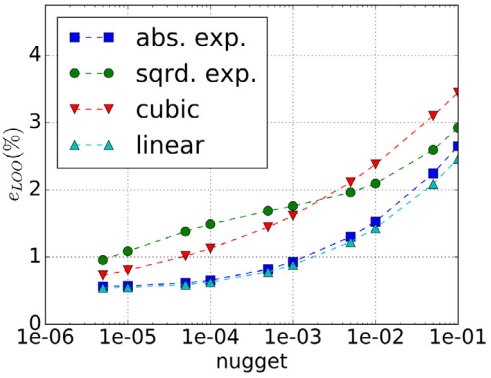

(c) Quadratic regression function

Fig. 13. Influence of regression function, correlation function and nugget value on e_{LOO} of the Kriging model for the core discharge coefficient C_D^{core} for engine E1.

sion associated to the bypass flow, which, in turn, is non-linear as it depends on the shock pattern on the core cowl (section 3.1). For engine E1, the best Kriging model gives a e_{LOO} of 0.003%, 0.003% and 0.5% for C_{F_x}, C_D^{bypass} and C_D^{core}, respectively.

The study of the Kriging model performance was carried out for engine E2, Figs. 14 to 16. Engine E2 is representative of current state of the art architectures and its exhaust system has different performance maps from those of engine E1 (section 3.2). For this engine too, the nugget values has a strong influence on e_{LOO} for C_{F_x} and C_D^{core}. Furthermore, the Kriging model provides relatively small errors. The smallest e_{LOO} for C_{F_x} and C_D^{core} is approximately 0.01% and 1.0%, respectively (Figs. 14 and 16). For C_D^{bypass}, which has small variations across the design space (section 3.2.2), the Kriging provides very small errors, with $e_{\text{LOO}} < 5 \times 10^{-5}\%$ for lower values of the nugget and for any correlation function (Fig. 15).

4.2. Radial basis functions

Radial Basis Functions can be considered a sub-class of generalized Kriging models as they are pure correlation functions [22]. In this work well-known basis functions are employed, Table 2. Furthermore, the closed form of the basis function model is obtained by imposing that the basis functions go through each point of the dataset exactly. Hence the resulting model behaves as pure interpolation, as opposed to Kriging which is a regression model.

The choice of the basis functions has clearly an impact on the accuracy of the resulting model, Fig. 17 and Fig. 18. The e_{LOO} is between 0.5% and 0.007% for C_{F_x} and C_D^{bypass}, while the error levels are between 2.5% and 0.4% for C_D^{core}. The Gaussian RBF consistently provided error levels almost an order of magnitude higher than the other basis functions. Consequently the data from the Gaussian RBF is not presented and its use is not recommended. For the datasets

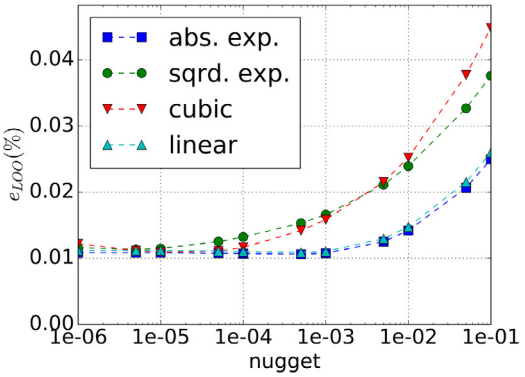

(a) Constant regression function

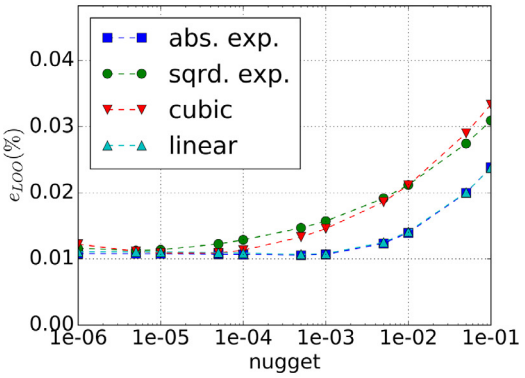

(b) Linear regression function

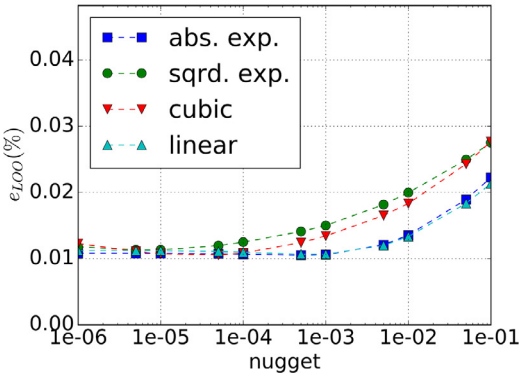

(c) Quadratic regression function

Fig. 14. Influence of regression function, correlation function and nugget value on e_{LOO} of the Kriging model for the axial force coefficient C_{F_x} for engine E2.

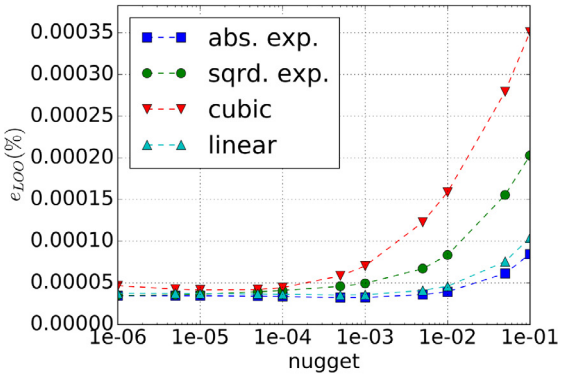

(a) Constant regression function

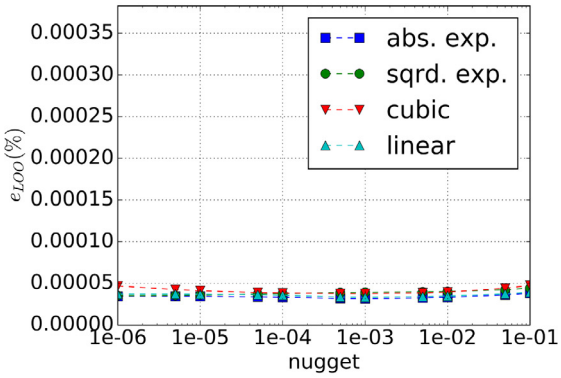

(b) Linear regression function

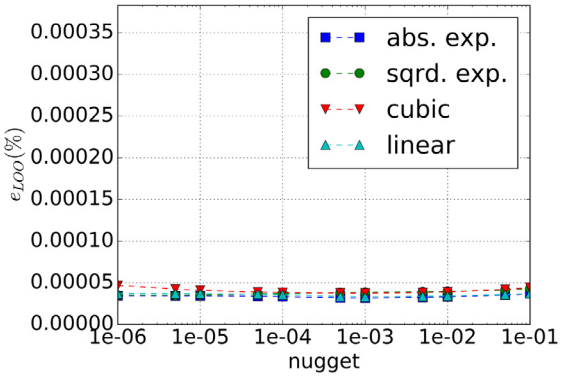

(c) Quadratic regression function

Fig. 15. Influence of regression function, correlation function and nugget value on e_{LOO} of the Kriging model for the bypass discharge coefficient C_D^{bypass} for engine E2.

presented in this work based on the exhaust system performance metrics, the better function is the quintic, which performs remarkably well for all metrics. The only exception is for C_D^{core} of engine E2, for which the multiquadratic RBF gives a better result than the quintic (Fig. 18b). For engine E1, the RBF surrogate model built with the quintic basis function gives a e_{LOO} of 0.007%, 0.008% and 0.4% for C_{F_x}, C_D^{bypass} and C_D^{core}, respectively. Similar albeit slightly higher values are obtained for engine E2. These values are comparable to those obtained using the Kriging model and within the CFD uncertainty reported in section 3.3.3. Hence both the Kriging and the RBF model are able to represent with sufficient accuracy the original dataset and the method is fit for the purpose, i.e. for the rapid assessment of performance metrics in the context of preliminary design.

4.3. Influence of the number of samples on the model accuracy

In order to gain understanding on how the accuracy of the model changes as a function of the number of samples, coarser datasets were defined and the model that gives the lowest e_{LOO} was identified for each coarse dataset.

For the engine E1, different coarsening strategies have been applied. Regardless of the coarsening strategy, the bounds of the design space have been kept fixed. A global coarsening has been performed, for which every other datapoint is selected from the original dataset of Ma_∞, FNPR and ER combinations. Furthermore, every other point of one variable at the time has been selected, so either coarsening the samples for Ma_∞, ER or FNPR. A summary of the resulting samples is given in Table 4.

For each coarse dataset, the quality of the corresponding surrogate models was quantified. First the best models of the two families, i.e. the models that provided the lowest e_{LOO}, were identified.

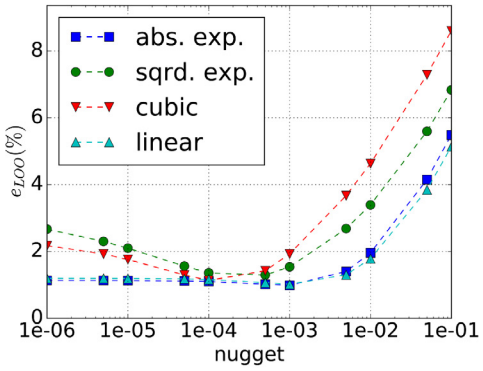

(a) Constant regression function

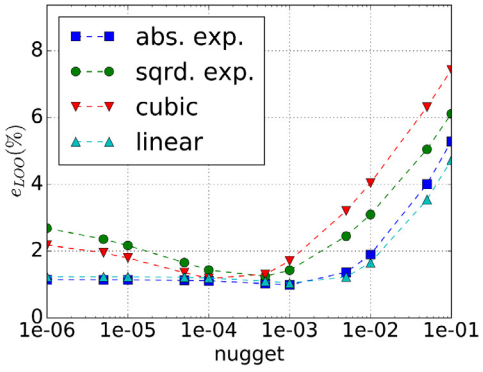

(b) Linear regression function

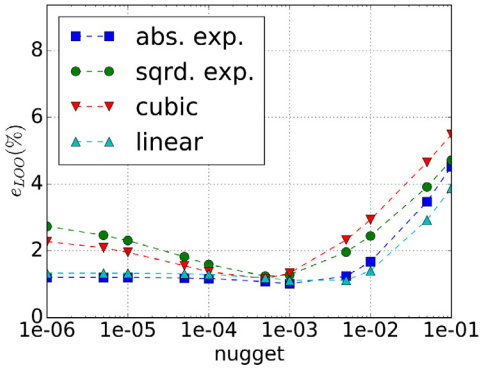

(c) Quadratic regression function

Fig. 16. Influence of regression function, correlation function and nugget value on e_{LOO} of the Kriging model for the core discharge coefficient C_D^{core} for engine E2.

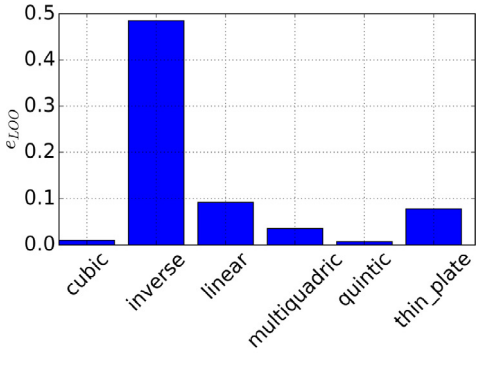

(a) C_{F_x}

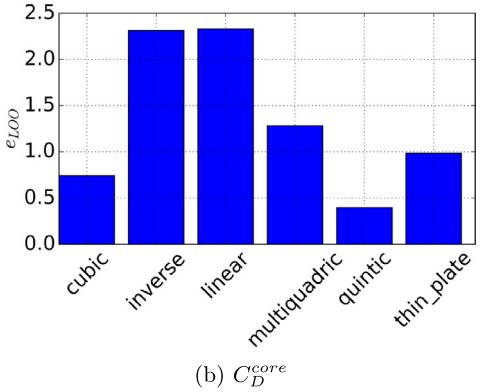

(b) C_D^{core}

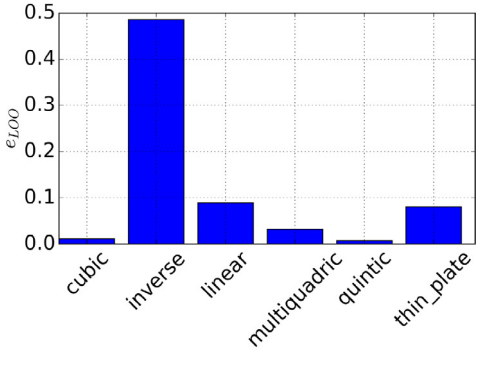

(c) C_D^{bypass}

Fig. 17. Influence of radial basis function on e_{LOO} (%) of the corresponding surrogate model for the three performance metrics for engine E1.

Table 4
Coarser datasets for engine E1.

Coarsening variable	Level	Ma_∞ samples	FNPR samples	ER samples	Total samples
none (finest dataset)	0	13	25	5	1625
Ma_∞, FNPR, ER	1	7	13	3	273
ER	1	13	25	3	975
FNPR	1	13	13	5	845
FNPR	2	13	7	5	455
Ma_∞	1	7	25	5	875
Ma_∞	2	4	25	5	500

For a Gaussian Process, this was done by studying the influence of the choices of the regression function, correlation function and nugget value. For RBFs, it was determined which of the radial basis function (Table 2) performed best. Once the best models of the two families had been identified, they were queried in each point of the finest dataset, and the RMS of the relative error, e_{finest}, was computed as in eq. (18):

$$e_{\text{finest}} = \sqrt{\frac{1}{N}\sum_{i=1}^{N}\left(\frac{\tilde{y}_i^{\text{coarse}} - y_i^{\text{CFD}}}{y_i^{\text{CFD}}}\right)^2} \tag{18}$$

where $\tilde{y}_i^{\text{coarse}}$ represent the result obtained by querying the RSM fitted on the given coarse dataset, and y_i^{CFD} is the reference result, i.e. that given by the CFD.

The RBF are pure correlation functions, thus the error with respect to the finest data set is always zero, Figs. 19 to 22. On the contrary, the Kriging model has an inherent non-zero error, albeit small, also when applied to the finest dataset. Furthermore, it has been shown before that the best results with the Kriging model are generally obtained for very small values of the nugget. The nugget value can be seen as a relaxation factor, the smaller its value the more the model is forced locally to recover the original datapoint. Thus, for the particular set of

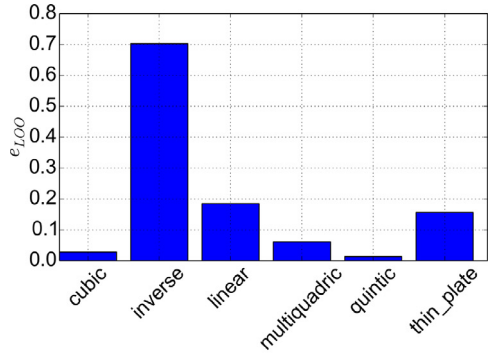

(a) C_{F_x}

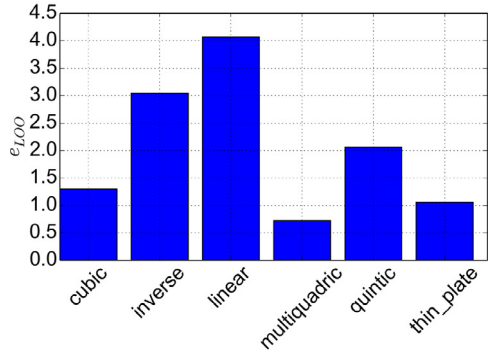

(b) C_D^{core}

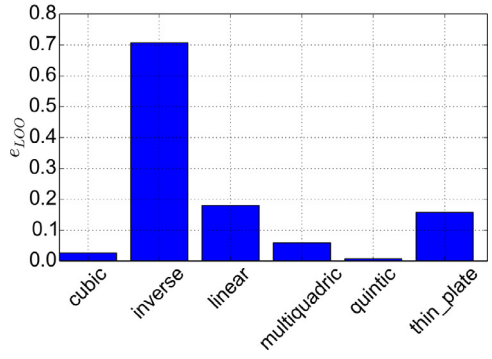

(c) C_D^{bypass}

Fig. 18. Influence of radial basis function on e_{LOO} (%) of the corresponding surrogate model for the three performance metrics for engine E2.

data analysed in this work, the best strategy is to have a relatively rigid model that almost goes through all the original datapoints. This happens exactly, by construction, in case of the RBF.

For engine E1, the two families of surrogate models perform similarly regarding C_{F_x}. For C_{F_x}, the error e_{finest} increases the most when performing a global coarsening, for which $e_{\text{finest}} \approx 0.35\%$ (Fig. 19a). By comparing Figs. 20a, 21a and 22a it can be seen that the main source of error comes from coarsening the datapoints for the variable Ma_∞. On the first of the coarser levels for Ma_∞ (Fig. 20a), the error e_{finest} is almost the same as the error obtained when performing a global coarsening (Fig. 19a). A coarsening for FNPR or ER gives error levels one order of magnitude smaller. This indicates that the input variable that has the largest impact on the quality of the RSM for C_{F_x} is the freestream Mach number Ma_∞. This is consistent with the trends observed in the performance maps showed in Fig. 4.

For C_D^{core}, focusing on the Kriging model, the main source of error comes from the coarsening of ER samples, which gives an error of $e_{\text{finest}} \approx 1.7\%$, Fig. 22b. The same tendency can be observed for the RBF, which however is more tolerant to the reduction of samples and the errors on the first coarser levels are always below 0.3%.

For C_D^{bypass} the errors are generally small for both Kriging and RBF, with $e_{\text{finest}} < 0.15\%$ even at the coarser level 2, see Figs. 19c, 20c, 21c and 22c. The error is manly influenced by the coarsening for FNPR and Ma_∞, while the coarsening of ER samples has the smallest impact. This is consistent with the performance map in Fig. 6 which shows that C_D^{bypass} is almost independent of ER. For the engine representative of future architectures E1, models with sufficient accuracy are obtained when one level of coarsening is applied to the variables FNPR or ER (Figs. 21 and 22).

5. Conclusions

The aim of this work was to assess the quality of surrogate models for the prediction of the performance of the exhaust system of civil aero-engines. In the context of preliminary design, the characteristics of the exhaust system is typically taken into account with relatively simple models, which are derived from inviscid relations applied to isolated nozzles. The method developed in this work expands the classical simple models by taking into account not only the fan nozzle pressure ratio, but also the free-stream Mach number and the extraction ratio.

Two families of surrogate models have been investigated, Kriging and RBF and they have been applied to data relative to two engines, one representative of the future turbofan very-high-bypass-ratio engines (E1) and one representative of the current state of the art (E2). The models have been fit to predict three main performance metrics: the overall axial force coefficient, the bypass discharge coefficient and core nozzle discharge coefficient. The database of results for each engine has been obtained via CFD simulations for wide ranges of operating conditions. For engine E1, the overall axial force coefficient and the bypass nozzle discharge coefficient are influenced mainly by the free-stream Mach number and by the nozzle pressure ratio. The core discharge coefficient is influenced considerably also by the extraction ratio. Similar considerations can be made for engine E2.

The quality of the models has been analysed in detail. Results show that with a careful tuning of the settings of the models, both families can achieve similar results in terms of quality of the model. In particular, for the Kriging model, it has been shown that the choice of the nugget value has a stronger influence than the choice of the regression and correlation functions. Regarding the RBF, the quintic radial basis function was the better suited for the dataset analysed in this work, as it consistently provided the highest quality of the corresponding surrogate model.

It has been shown that the studied method is able to accurately predict the nozzle performance characteristics. For engine E1, the Kriging model fit using the finest dataset (1625 samples) gave an estimated average error of 0.003%, 0.003% and 0.50% for C_{F_x}, C_D^{bypass} and C_D^{core}, respectively. Similar results were obtained with the RBF. For engine E2, the Kriging model trained on a dataset of 663 samples produced errors of 0.011%, 3.1×10^{-5}% and 0.98% for C_{F_x}, C_D^{bypass} and C_D^{core}, respectively. The RBF model gave similar results. These estimated average errors are within the error levels found in literature relating CFD to experiments of nozzles, thus the method is considered fit for the purpose. Future work includes the investigation of new classes of engines, wider operational envelope and more advanced sampling techniques.

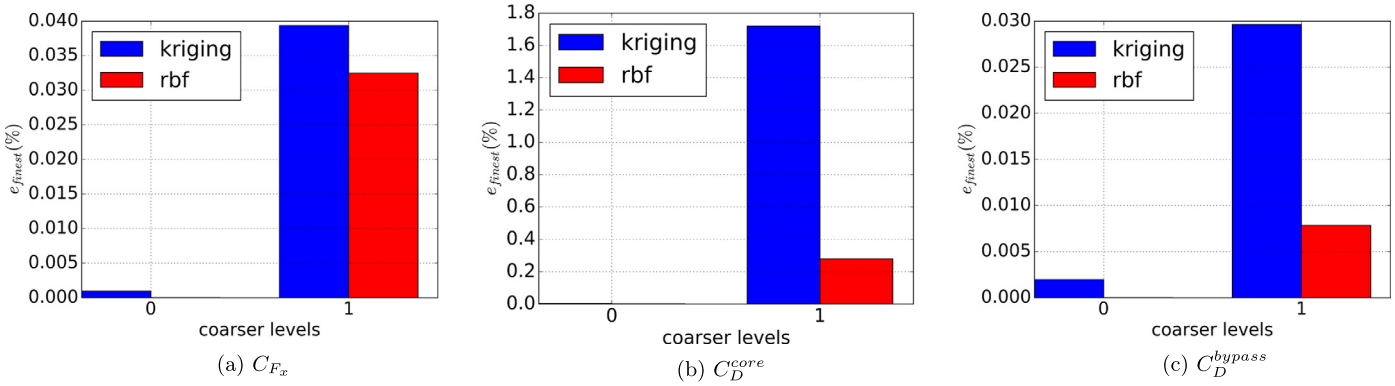

(a) C_{F_x} (b) C_D^{core} (c) C_D^{bypass}

Fig. 19. Influence of the number of samples on the error with respect to the finest dataset e_{finest} for engine E1. Coarser levels obtained by taking every other point for all three variables, Ma_∞, FNPR and ER, at the same time (global coarsening).

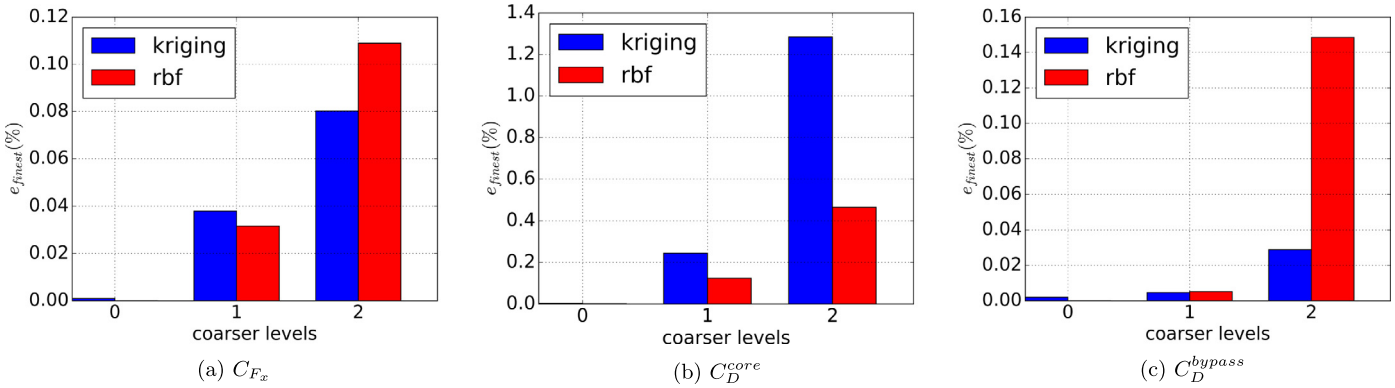

(a) C_{F_x} (b) C_D^{core} (c) C_D^{bypass}

Fig. 20. Influence of the number of samples on the error with respect to the finest dataset e_{finest} for engine E1. Coarser levels obtained by taking every other point for Ma_∞.

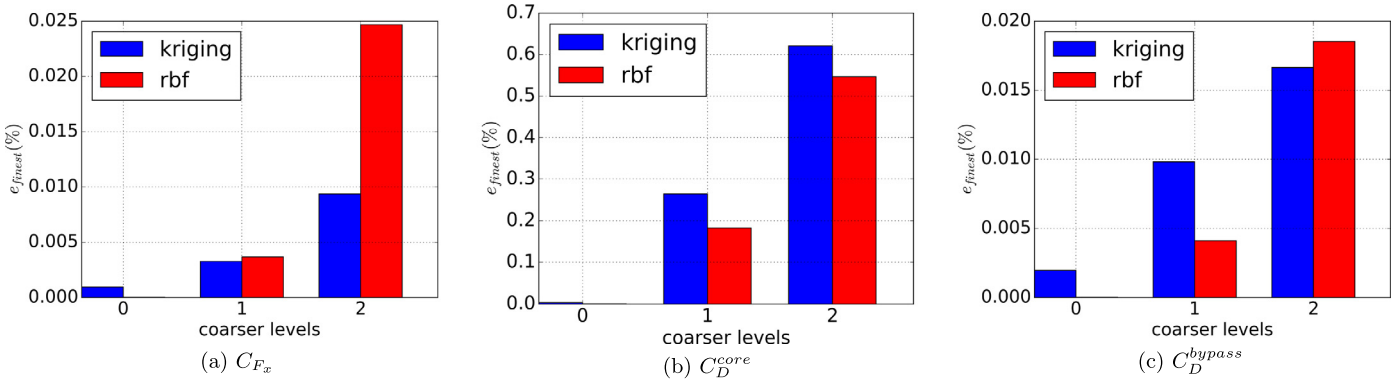

(a) C_{F_x} (b) C_D^{core} (c) C_D^{bypass}

Fig. 21. Influence of the number of samples on the error with respect to the finest dataset e_{finest} for engine E1. Coarser levels obtained by taking every other point for FNPR.

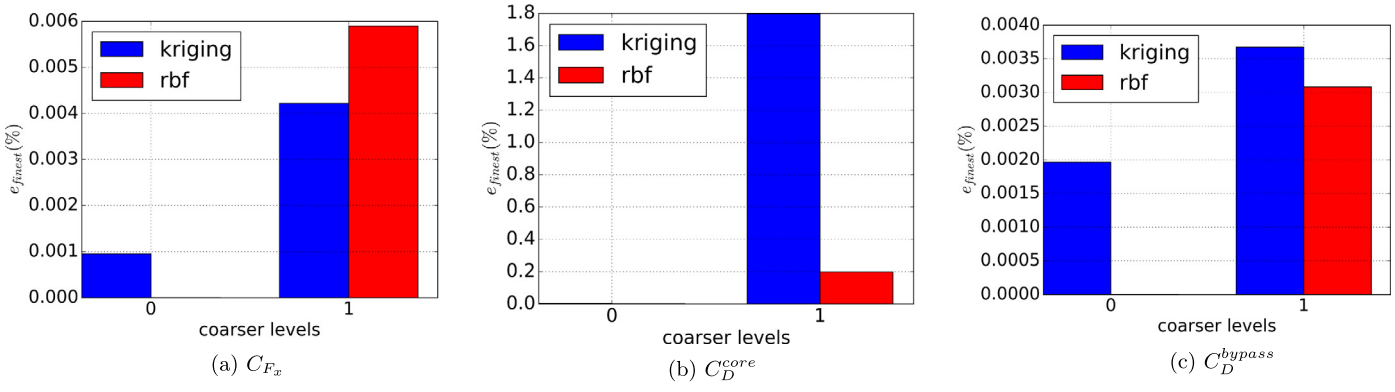

(a) C_{F_x} (b) C_D^{core} (c) C_D^{bypass}

Fig. 22. Influence of the number of samples on the error with respect to the finest dataset e_{finest} for engine E1. Coarser levels obtained by taking every other point for ER.

Data statement

Due to commercial confidentiality agreements the supporting data is not available.

Declaration of Competing Interest

There is no competing interest.

Acknowledgements

This work was co-funded by Innovate UK, APROCONE project, reference TSB113092.

References

[1] I. Goulos, T. Stankowski, J. Otter, D. MacManus, N. Grech, C. Sheaf, Aerodynamic design of separate-jet exhausts for future civil aero-engines—Part I: parametric geometry definition and computational fluid dynamics approach, J. Eng. Gas Turbines Power 138 (8) (2016) 081201.
[2] P.P. Walsh, P. Fletcher, Gas Turbine Performance, John Wiley & Sons, 2004.
[3] J. Mattingly, Elements of Gas Turbine Propulsion, AIAA Education Series, American Institute of Aeronautics and Astronautics, 2005.
[4] G.C. Oates, Aircraft Propulsion Systems Technology and Design, American Institute of Aeronautics and Astronautics, 1989.
[5] J.D. Anderson, Modern Compressible Flow, with Historical Perspective, McGraw-Hill, 1990.
[6] GasTurb GmbH, GasTurb 13, Design and Off-Design Performance of Gas Turbines v13, 2018.
[7] A. Alexiou, T. Tsalavoutas, TURBO 3.2 Library, PROOSIS (PRopulsion Object Oriented SImulation Software) v3.6.14, 2013.
[8] J.W. Chapman, T.M. Lavelle, J.S. Litt, Practical techniques for modeling gas turbine engine performance, in: AIAA Paper 2106-4527, 52nd AIAA/SAE/ASEE Joint Propulsion Conference, 2016.
[9] I. Goulos, J. Otter, T. Stankowski, D. MacManus, N. Grech, C. Sheaf, Aerodynamic design of separate-jet exhausts for future civil aero-engines—Part II: design space exploration, surrogate modeling, and optimization, J. Eng. Gas Turbines Power 138 (8) (2016) 081202.
[10] R. Johnson, The Handbook of Fluid Dynamics, Mechanical Engineering, Springer Berlin Heidelberg, 1998.
[11] K.L. Mikkelsen, D.J. Myren, D.G. Dahl, M. Christiansen, Initial subscale performance measurements of the AIAA Dual Separate Flow Reference DSFR nozzle, in: AIAA Paper 2015-3883, 51st AIAA/SAE/ASEE Joint Propulsion Conference, 2015.
[12] M.H. Robinson, D.G. MacManus, K. Richards, C. Sheaf, Short and slim nacelle design for ultra-high BPR engines, in: AIAA Paper 2017-0707, 55th AIAA Aerospace Sciences Meeting, 2017.
[13] J.J. Otter, I. Goulos, D.G. MacManus, M. Slaby, Aerodynamic analysis of civil aeroengine exhaust systems using computational fluid dynamics, J. Propuls. Power 34 (5) (2018) 1152–1165.
[14] A. Heidebrecht, D.G. MacManus, Surrogate model of complex non-linear data for preliminary nacelle design, Aerosp. Sci. Technol. 84 (2019) 399–411.
[15] T. Mackman, C. Allen, M. Ghoreyshi, K. Badcock, Comparison of adaptive sampling methods for generation of surrogate aerodynamic models, AIAA J. 51 (4) (2013) 797–808.
[16] Z.-H. Han, S. Görtz, R. Zimmermann, Improving variable-fidelity surrogate modeling via gradient-enhanced kriging and a generalized hybrid bridge function, Aerosp. Sci. Technol. 25 (1) (2013) 177–189.
[17] S. Bhattrai, J.H. de Baar, A.J. Neely, Efficient uncertainty quantification for a hypersonic trailing-edge flap, using gradient-enhanced kriging, Aerosp. Sci. Technol. 80 (2018) 261–268.
[18] K.L. Mikkelsen, T.J. McDonald, N. Saiyed, Static and wind tunnel aeroperformance tests of nasa ast separate flow nozzle noise reduction configurations, in: NASA Technical Report NASA/CR-2001-210712, E-12658, NAS 1.26:210712, 2001.
[19] B.M. Kulfan, Universal parametric geometry representation method, J. Aircr. 45 (1) (2008) 142–158.
[20] P. Roache, Perspective: a method for uniform reporting of grid refinement studies, J. Fluids Eng. 116 (3) (1994) 405–413.
[21] J. Helton, F. Davis, Latin hypercube sampling and the propagation of uncertainty in analyses of complex systems, Reliab. Eng. Syst. Saf. 81 (1) (2003) 23–69.
[22] A. Forrester, A. Sóbester, A. Keane, Engineering Design Via Surrogate Modelling: A Practical Guide, John Wiley & Sons, 2008.
[23] S.N. Lophaven, H.B. Nielsen, J. Søndergaard, DACE: a MatLab Kriging Toolbox, Technical Report IMM-TR-2002-12, 2002, http://www2.imm.dtu.dk/projects/dace/dace.pdf.
[24] M.D. Buhmann, Radial Basis Functions: Theory and Implementations, Cambridge University Press, 2003.
[25] E. Jones, T. Oliphant, P. Peterson, et al., SciPy: open source scientific tools for Python, [Online, accessed 21/05/2018] (2001–), http://www.scipy.org/.
[26] F. Pedregosa, G. Varoquaux, A. Gramfort, V. Michel, B. Thirion, O. Grisel, M. Blondel, P. Prettenhofer, R. Weiss, V. Dubourg, J. Vanderplas, A. Passos, D. Cournapeau, M. Brucher, M. Perrot, E. Duchesnay, Scikit-learn: machine learning in Python, J. Mach. Learn. Res. 12 (2011) 2825–2830.
[27] R. Kohavi, A study of cross-validation and bootstrap for accuracy estimation and model selection, in: 14th International Joint Conference on Artificial Intelligence (IJCAI95), Montreal, Canada, vol. 14, 1995, pp. 1137–1145.